Biophysical Journal
Article

Biophysical Society

Inference of Internal Stress in a Cell Monolayer

Vincent Nier,[1] Shreyansh Jain,[2] Chwee Teck Lim,[2,3] Shuji Ishihara,[4] Benoit Ladoux,[2,5] and Philippe Marcq[1,*]
[1]Sorbonne Universités, UPMC, Université Paris 6, Institut Curie, Centre National de la Recherche Scientifique, UMR 168, Laboratoire Physico-Chime Curie, Paris, France; [2]Mechanobiology Institute, National University of Singapore, Singapore; [3]Department of Biomedical Engineering and Department of Mechanical Engineering, National University of Singapore, Singapore; [4]Department of Physics, Meiji University, Kawasaki, Kanagawa, Japan; and [5]Institut Jacques Monod, Centre National de la Recherche Scientifique, UMR 7592, Université Paris Diderot, Paris, France

ABSTRACT We combine traction force data with Bayesian inversion to obtain an absolute estimate of the internal stress field of a cell monolayer. The method, Bayesian inversion stress microscopy, is validated using numerical simulations performed in a wide range of conditions. It is robust to changes in each ingredient of the underlying statistical model. Importantly, its accuracy does not depend on the rheology of the tissue. We apply Bayesian inversion stress microscopy to experimental traction force data measured in a narrow ring of cohesive epithelial cells, and check that the inferred stress field coincides with that obtained by direct spatial integration of the traction force data in this quasi one-dimensional geometry.

INTRODUCTION

Dynamical behaviors of multicellular assemblies play a crucial role during tissue development (1) and in the maintenance of adult tissues (2). In addition, disregulation of multicellular structures may lead to pathological situations such as tumor formation and tumor progression (3). In this context, cell monolayers have been extensively studied to model in vivo tissue functions. Such approaches allow for well-controlled experiments, which have been performed in a variety of settings, such as monolayer spreading (4,5), wound healing (6,7), channel flow (8,9), confined flow (10,11), and collective migration (12,13). The dynamics of multicellular assemblies is regulated through mechanical forces that act upon cell adhesive structures. These forces are exerted at the cell-substrate interface (14), but also through cell-cell junctions (15). The transmission of stresses within multicellular assemblies is thus important to understand collective movements, cell rearrangements, and tissue homeostasis. Even though kinematic information is readily available, mechanical properties that rely on internal stress are less well understood. Indeed a number of important biological questions, such as the determination of the molecular mechanisms that underlie the transmission of force within a tissue (16), necessitate a measurement of internal stresses.

Several internal force measurement methods have been proposed and implemented (see Sugimura et al. (17) for a recent review): at the molecular scale, Förster resonance energy transfer (18,19); at the cell scale, microrheology (20,21); and at the tissue scale, liquid drops (22), birefringence (23), or laser ablation (24,25). Although one would ideally like to read out from data the spatio-temporal dependence of the full stress field, the above methods yield either a local, subtissue scale measurement (18–22), or a subset of the components of the stress tensor (23), or a relative measurement—up to an undetermined multiplicative constant (24,25). Monolayer stress microscopy (MSM), first introduced in Tambe et al. (26), does not suffer from these drawbacks: it builds upon the measurement of traction force data to estimate the stress field of monolayers of cohesive cells. Indeed, the force exerted by cells on a planar-deformable substrate can be computed from the displacement field of the underlying layer (27,28), using either: (1) traction force microscopy (5,29,30) where small beads are inserted within the (elastic) substrate, their displacements are measured, and the traction forces are obtained by solving an inverse elastic problem; or (2) arrays of micropillars (31–33), where the traction forces are simply proportional to the in-plane displacements of the pillars. However, once the traction forces are known, obtaining the internal stress from the force balance equations is an underdetermined problem because, in the two-dimensional case, three components of the symmetrical stress tensor must be obtained from two traction force components. In MSM (26,34), these equations become well-posed thanks to an additional hypothesis on tissue rheology: the cell monolayer is assumed to be a linear, isotropic elastic body. MSM has been validated

Submitted October 16, 2015, and accepted for publication March 7, 2016.
*Correspondence: philippe.marcq@curie.fr
Editor: Cecile Sykes.
http://dx.doi.org/10.1016/j.bpj.2016.03.002

independently on numerical data using particle dynamics simulations: in Zimmermann et al. (35), the reasonable accuracy of stress reconstruction from data that does not correspond to an elastic rheology has been attributed to the weakness of shear stresses in both simulated and living tissues. Assuming again that the tissue is an elastic body, and in addition that the displacement field is continuous at the cell-substrate interface, internal stresses may also be computed directly from substrate displacement data, circumventing the need to compute traction forces (36).

In the presence of cell divisions and extrusions that constantly rearrange a tissue (37), it is not clear that its rheology is that of a solid body. To our knowledge, the elastic rheology hypothesis has not been directly validated, while alternative rheologies have been proposed in the literature (7,38–40) and shown to model successfully specific aspects of the mechanical behavior of cell monolayers. Further, the rheology of multicellular assemblies may depend on the timescale (37), as well as on the type of cell considered (41). These caveats call for a method to accurately estimate the internal stress field of a cell monolayer irrespective of the underlying rheology.

A classical way to solve underdetermined inversion problems involves Bayesian inference (42), a technique originating in statistics (43), and now widely used in physics (44) and biophysics (45). Of note, Bayesian inversion has also been used to solve the inverse elastic problem of traction force microscopy (46,47). Recently, some among us proposed a Bayesian force inference method based on cell geometry, and applied it to segmented images of the *Drosophila* pupal wing and notum (48–50). The tissue-scale stress arises from coarse-graining of cell-cell interactions. For tight epithelia where adherens junctions are a key player of force transmission between neighboring cells, it is reasonable to assume that the cell-scale contribution to stress is mostly related to local contact within the apical side of the epithelium, whereas basal contributions from, e.g., lamellipodia, are negligible. Accordingly, the dominant contributors to tissue-scale stress were identified as cell pressures and cell-cell junction tensions, and force balance equations were written at each cell vertex, resulting in an underdetermined system. This system was solved using Bayesian inversion (42), where the inferred tensions and pressures were the most likely values (the modes) of a posterior distribution function. In the case of the fruitfly pupal wing, it turned out that tissue stress, obtained by coarse-graining, is oriented by external forces, and that its anisotropy promotes hexagonal cell packing (49). Similar systems of equations may become well-posed thanks to additional hypotheses (equal cell pressures (50,51)), or when cell pressures are not required (52). However, the stress is measured up to an arbitrary additive constant: its absolute value is out of reach because the input data are cell vertex positions and cell junction angles.

Below, we formulate Bayesian inversion stress microscopy (BISM), a method to estimate the internal stress field of a cell monolayer from traction-force microscopy measurements. Importantly, BISM yields an absolute measure of the stress and dispenses with hypotheses on monolayer rheology. We define BISM and introduce statistical measures of its accuracy. The method is first validated using numerical simulations that provide traction-force data. The inferred stress field, once computed, is compared to the simulated stress data used as a reference. Robustness is checked by implementing changes in the statistical model, as well as in the mechanical ingredients of the numerical simulations. BISM is further validated using experimental data in a quasi one-dimensional (1D) geometry that allows for a direct calculation of the stress field by spatial integration of the traction force field. Finally, our results are compared with existing methods.

MATERIALS AND METHODS

Mechanics

Within a continuum description, a flat, thin cell monolayer is characterized at position $\vec{r}$ and time t by a field of two-dimensional internal stresses $\sigma(\vec{r},t)$ and by a field of external surfacic forces $\vec{t}(\vec{r},t)$ that the monolayer exerts on the substrate. Because inertia is negligible, the balance of linear momentum reads in vector form

$$\mathrm{div}\ \sigma = \vec{t}, \tag{1}$$

and in Cartesian coordinates (x,y) (see S1.2 in the Supporting Material for polar coordinates)

$$\frac{\partial \sigma_{xx}}{\partial x} + \frac{\partial \sigma_{xy}}{\partial y} = t_x, \tag{2}$$

$$\frac{\partial \sigma_{yx}}{\partial x} + \frac{\partial \sigma_{yy}}{\partial y} = t_y. \tag{3}$$

Note that at this stage, due to the grid definition (see below and Fig. 1 *b*), we do not enforce the symmetry of the stress tensor (equality of the shear stress components due to angular momentum conservation (53)). With a confined monolayer in mind (10,11), the boundary condition reads

$$\sigma_{ij}\, n_j = 0, \tag{4}$$

where $\vec{n}$ denotes the vector normal to the edge, and summation over repeated indices is implied. In the plane, the units of stresses and (surfacic) forces are Pa.m and Pa, respectively. Assuming that the monolayer height is uniform and constant $h(\vec{r},t) = h_0$, the 3D stress reads $\sigma_{3D} = \sigma/h_0$. When spatial or temporal variations of the height cannot be neglected (4,5), BISM can be implemented by replacing $\vec{t}(\vec{r},t)$ by $\vec{t}(\vec{r},t)/h(\vec{r},t)$ and by inferring the 3D stress from $\mathrm{div}\ \sigma_{3D} = \vec{t}/h$, provided that the height remains small compared to the system size, as is generally the case for in vitro cell monolayers (26,54). A treatment of the full 3D case where the height is comparable or larger than the system size is beyond the scope of this work.

Because experimental traction forces are measured with a finite spatial resolution l, assumed to be isotropic for simplicity, we write a force balance equation in each of a large number of square surface elements of area l^2 (see Fig. 1 *a*). We aim at inferring the stress tensor $\sigma(i,j) = \begin{pmatrix} \sigma_{xx}(i,j) & \sigma_{yx}(i,j) \\ \sigma_{xy}(i,j) & \sigma_{yy}(i,j) \end{pmatrix}$ in each element. The traction force exerted by the tissue in element (i,j) on the substrate is $\vec{t}(i,j)$, with components

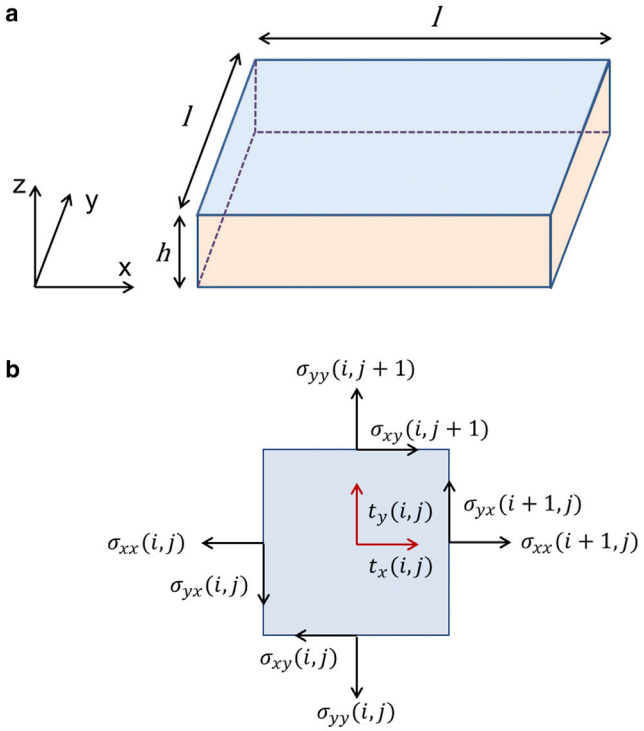

FIGURE 1 Discrete monolayer mechanics. (*a*) A tissue element of volume $l^2 \times h$. (*b*) Pictorial representation of local force balance; see Eqs. 5 and 6, and see text for definitions. To see this figure in color, go online.

$t_x(i,j), t_y(i,j)$. In the case of a rectangular grid with C columns and R rows, the discretized force balance equation for element (i,j) reads

$$l\left[\sigma_{xx}(i+1,j) - \sigma_{xx}(i,j) + \sigma_{xy}(i,j+1) - \sigma_{xy}(i,j)\right] = l^2\, t_x(i,j), \tag{5}$$

$$l\left[\sigma_{yx}(i+1,j) - \sigma_{yx}(i,j) + \sigma_{yy}(i,j+1) - \sigma_{yy}(i,j)\right] = l^2\, t_y(i,j) \tag{6}$$

to lowest order in l (see Fig. 1 *b*). We thus have $N = C \times R$ variables for t_x and t_y, $(C+1) \times R$ variables for σ_{xx} and σ_{yx} and $C \times (R+1)$ variables for σ_{yy} and σ_{xy}. Defining traction force and stress vectors as

$$\vec{T} = \left[t_x(1,1)\cdots t_x(R,C)\; t_y(1,1)\cdots t_y(R,C)\right]^t,$$

$$\vec{\sigma} = \left[\sigma_{xx}(1,1)\cdots\sigma_{xx}(C+1,R)\;\sigma_{yy}(1,1)\cdots\sigma_{yy}(C,R+1) \times \sigma_{xy}(1,1)\cdots\sigma_{xy}(C,R+1)\;\sigma_{yx}(1,1)\cdots\sigma_{yx}(C+1,R)\right]^t,$$

where the superscript t denotes the transpose, we rewrite Eqs. 5 and 6 in matrix form

$$A\,\vec{\sigma} = \vec{T}. \tag{7}$$

The matrix A, of size $2N \times (4N + 2(C+R))$, may be decomposed as

$$A = \begin{pmatrix} A_x & 0 & A_y & 0 \\ 0 & A_y & 0 & A_x \end{pmatrix}, \tag{8}$$

where A_x and A_y correspond to the discretized matrix forms, at second order in l, of the partial derivatives with respect to x and y.

Statistics

To solve the underdetermined linear system (Eq. 7), we implement Bayesian inversion (42): all variables and parameters of the problem are probabilized. For simplicity, we use, wherever possible, Gaussian probability distribution functions, denoted $\mathcal{N}(\vec{X}\,|\,\vec{m}, S)$ for a multivariate (vector) Gaussian random variable $\vec{X}$ with mean $\vec{m}$ and covariance matrix S.

Likelihood

The first ingredient of the statistical model is the likelihood function $L(\vec{T}\,|\,\vec{\sigma})$, which contains information provided by experimental measurements. For experimental data, the force balance equations (Eq. 7) are verified up to an additive noise due to measurement errors. Assuming this noise to be Gaussian with zero mean and uniform covariance matrix $S = s^2\, I$, where the parameter s^2 denotes the noise variance and I is the identity matrix, the likelihood is expressed as $L(\vec{T}\,|\,\vec{\sigma}) = \mathcal{N}(\vec{T}\,|\,A\vec{\sigma}, s^2\, I)$ or

$$L(\vec{T}\,|\,\vec{\sigma}) = \left(\frac{1}{\sqrt{2\pi s^2}}\right)^{2N} \exp\left[-\frac{||\vec{T}-A\vec{\sigma}||^2}{2s^2}\right], \tag{9}$$

where $\|\ldots\|$ is the (L_2) Euclidean norm.

Prior

Second, the prior probability distribution function $\pi(\vec{\sigma})$ embeds additional information concerning the stress field:

(1) We assume that the stress obeys a Gaussian distribution function with zero mean $\vec{\sigma}_0 = \vec{0}$ and covariance matrix $s_0^2\, I$;
(2) We enforce the equality of the two off-diagonal components of the stress tensor: in compact vector form $\vec{\sigma}_{xy} = \vec{\sigma}_{yx}$, i.e., $\sigma_{xy}(i,j) + \sigma_{xy}(i,j+1) = \sigma_{yx}(i,j) + \sigma_{yx}(i+1,j)\ \forall(i,j)$ (see Fig. 1 *b* and S1.3);
(3) We enforce the boundary conditions (Eq. 4), namely two conditions at each boundary element (i,j), written in compact vector form $\vec{\sigma}_{BC} = \vec{0}$).

Up to a normalizing factor, the prior reads

$$\pi(\vec{\sigma}) \propto \exp\left[-\frac{\|\vec{\sigma}\|^2 + \alpha_{xy}^2\|\vec{\sigma}_{xy} - \vec{\sigma}_{yx}\|^2 + \alpha_{BC}^2\|\vec{\sigma}_{BC}\|^2}{2s_0^2}\right] \tag{10}$$

or

$$\pi(\vec{\sigma}) = \left(\frac{1}{\sqrt{2\pi\,|B|\,s_0^2}}\right)^{4N+2(R+C)} \exp\left[-\frac{\vec{\sigma}^t B^{-1}\vec{\sigma}}{2s_0^2}\right]. \tag{11}$$

The second ingredient of the statistical model is a Gaussian prior $\pi(\vec{\sigma}) = \mathcal{N}(\vec{\sigma}\,|\,\vec{0}, S_0 = s_0^2\, B)$, where B is a reduced covariance matrix of determinant $|B|$. Note that a Gaussian prior suppresses stress values larger than a few times s_0 (see Schwarz et al. (55) for a similar approach in the context of traction force microscopy). In practice, we set the hyperparameters α_{xy} and α_{BC} to the values $\alpha_{xy} = \alpha_{BC} = 10^3$, large enough for conditions (2) and (3) to be enforced (see S3.2 for a discussion of these values). If required by a given experimental setup, the boundary conditions should be modified appropriately in the definition of the prior.

Resolution

According to Bayes' theorem, the posterior (conditional) probability distribution function $\Pi(\vec{\sigma}\,|\,\vec{T})$ of the stress given the traction force data is proportional to the product of the likelihood by the prior,

$$\Pi\left(\vec{\sigma}\,|\,\vec{T}\right) \propto L\left(\vec{T}\,\middle|\,\vec{\sigma}\right) \times \pi(\vec{\sigma}). \tag{12}$$

Because both are Gaussian, the posterior is also Gaussian $\Pi(\vec{\sigma}\,|\,\vec{T}) = \mathcal{N}(\vec{\sigma}\,|\,\vec{\sigma}_\Pi, S_\Pi)$, with a covariance matrix S_Π and a mean $\vec{\sigma}_\Pi$ given by (42)

$$S_\Pi = \left(S_0^{-1} + A^t\, S^{-1}\, A\right)^{-1}, \tag{13}$$

$$\vec{\sigma}_\Pi = S_\Pi\, A^t\, S^{-1}\, \vec{T}. \tag{14}$$

We use maximum a posteriori (MAP) estimation (42) and define the inferred stress $\widehat{\vec{\sigma}}$ as the mode (maximal value) of the posterior $\widehat{\vec{\sigma}} = \vec{\sigma}_\Pi$. Qualitatively, the underdeterminacy has been lifted: $4N + 2(R + C)$ unknown stress values are determined from $2N$ traction force values, $4N + 2(R + C)$ conditions from the Gaussian distribution of the stress tensor, N equalities of the two shear components, and $4(R + C)$ boundary conditions.

In this Gaussian model, MAP estimation is identical to minimization of a Tikhonov potential (42). The dimensionless regularization parameter

$$\Lambda = \frac{l^2\, s^2}{s_0^2} \tag{15}$$

quantifies the relative weight given to the prior, compared to the likelihood, when performing Bayesian inversion. Factoring out $(sl)^2$, Eqs. 13 and 14 read

$$S_\Pi = (sl)^2\left(\Lambda\, B^{-1} + l^2\, A^t\, A\right)^{-1}, \tag{16}$$

$$\vec{\sigma}_\Pi = \left(\Lambda\, B^{-1} + l^2\, A^t\, A\right)^{-1} l^2\; A^t\, \vec{T}. \tag{17}$$

Because the product Al is dimensionless and independent of l, the posterior covariance (Eq. 16) is a function of Λ and sl, while the posterior mode (Eq. 17) depends upon Λ and $l\vec{T}$.

Hyperprior

For generality's sake, we probabilize the parameter s^2 and the hyperparameter s_0^2, yet undetermined in Eqs. 13 and 14 (recall that $S = s^2\, I$ and $S_0 = s_0^2\, B$). Within the framework of hierarchical Bayesian descriptions, the model is closed by the hyperprior probability distribution functions $H(s^2)$ and $H(s_0^2)$ (56,57). Up to a normalizing factor, the posterior now reads (see Fig. 2 *a*)

$$\Pi\left(\vec{\sigma}\,|\,\vec{T}\right) \propto L\left(\vec{T}\,\middle|\,\vec{\sigma}, s^2\right) \times \pi\left(\vec{\sigma}\,\middle|\,s_0^2\right) \times H\left(s^2\right) \times H\left(s_0^2\right). \tag{18}$$

For simplicity, we use Jeffreys' noninformative hyperprior: $H(s^2) \propto 1/s^2$, $H(s_0^2) \propto 1/s_0^2$ (56,57).

Simultaneous a posteriori optimization with respect to $\vec{\sigma}$, s^2 and with s_0^2 being intractable, we solve the problem iteratively, starting from initial values $s^2_{(0)}$ and $s^2_{0(0)}$ (see Fig. 2 *b*). At step $k \geq 1$, we first calculate the mode $\vec{\sigma}_{\Pi\,(k)}$ from previous values $s^2_{(k-1)}$, $s^2_{0(k-1)}$ (Eqs. 13 and 14). Maximizing the posterior with respect to each hyperparameter yields the updated hyperparameter values

$$s^2_{(k)} = \tfrac{1}{2N+2}\left|\left|\vec{T} - A\vec{\sigma}_{\Pi\,(k)}\right|\right|^2, \tag{19}$$

$$s^2_{0(k)} = \tfrac{1}{4N+2(R+C)+2}\;\vec{\sigma}^{\,t}_{\Pi\,(k)}\, B^{-1}\, \vec{\sigma}_{\Pi\,(k)}. \tag{20}$$

Once convergence is reached, $s^2_{(k)} \to s^2_{(\infty)}$, $s^2_{0(k)} \to s^2_{0(\infty)}$, the stress estimate is defined as $\widehat{\vec{\sigma}} = \vec{\sigma}_{\Pi\,(\infty)}$, computed from Eqs. 13 and 14 with the optimal values $s^2_{(\infty)}$ and $s^2_{0(\infty)}$. An estimate $\delta\widehat{\vec{\sigma}}$ of the error on $\widehat{\vec{\sigma}}$ is calculated as the square root of the diagonal values of the covariance matrix $S_{\Pi\,(\infty)}$. Because the marginal distribution of traction forces is Gaussian, with a covariance matrix $S_T = S + A\, S_0\, A^t$ (42), we also calculate an estimate $\delta\widehat{T}$ of the error on the traction force as the square root of the diagonal values of S_T.

Measures of accuracy

The numerical resolution of a set of hydrodynamical equations yields a numerical data set $\{t^{\text{num}}\}$ of traction forces, from which we compute a set $\{\sigma^{\text{inf}}\}$ of inferred stresses. Because the numerical data set $\{\sigma^{\text{num}}\}$ of stresses is also available, measures of accuracy involving numerical simulations typically compare $\{\sigma^{\text{inf}}\}$ with $\{\sigma^{\text{num}}\}$.

A classical goodness-of-fit measure is the coefficient of determination, defined for the σ_{xx} component of the stress as

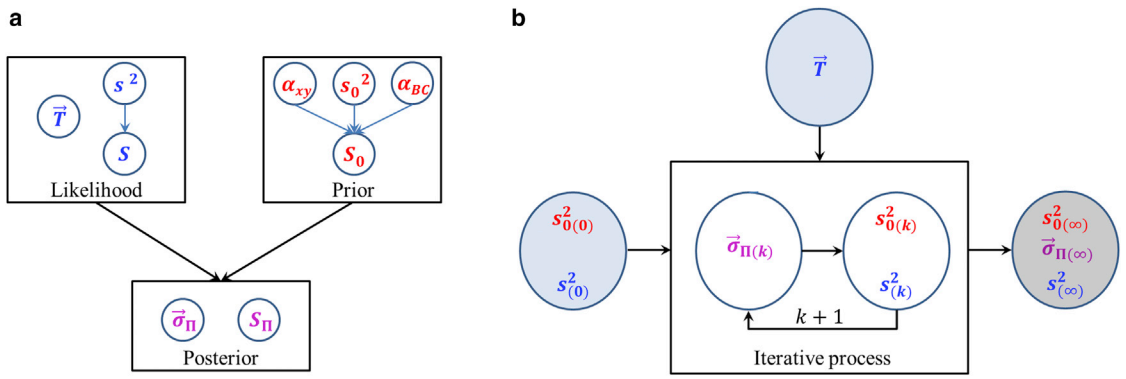

FIGURE 2 Schematics of BISM. (*a*) Both the likelihood (with parameter s^2), and the prior (with hyperparameters s_0^2, α_{xy}, and α_{BC}) contribute to the definition of the posterior, a Gaussian distribution function of mean $\vec{\sigma}_\Pi$, and covariance matrix S_Π. Given numerical values of s^2, s_0^2, α_{xy}, and α_{BC}, the MAP estimator of the stress $\widehat{\vec{\sigma}}$ is the mode of the posterior $\vec{\sigma}_\Pi$, Eq. 14. (*b*) In BISM, the values of s^2 and s_0^2 are not given a priori, but determined self-consistently within a hierarchical Bayesian construction. MAP estimation is performed iteratively, by successively optimizing the posterior for the mode $\vec{\sigma}_{(k)}$ (Eqs. 13 and 14) and for the variances $s^2_{(k)}$, $s^2_{0(k)}$ (Eqs. 19 and 20) until convergence to a fixed point is reached. The estimator of the stress $\widehat{\vec{\sigma}}$ is defined as the asymptotic value $\vec{\sigma}_{\Pi(\infty)}$, computed using $s^2_{(\infty)} = \lim_{k\to\infty} s^2_{(k)}$ and $s^2_{0(\infty)} = \lim_{k\to\infty} s^2_{0\,(k)}$ in Eqs. 13 and 14, with a regularization parameter $\Lambda_{(\infty)} = l^2\, s^2_{(\infty)}/s^2_{0\,(\infty)}$. A flowchart of the algorithm is given in Fig. S6. To see this figure in color, go online.

$$R^2_{xx} = 1 - \frac{\sum \left(\sigma^{\text{num}}_{xx} - \sigma^{\text{inf}}_{xx}\right)^2}{\sum \left(\sigma^{\text{num}}_{xx} - \left\langle \sigma^{\text{num}}_{xx} \right\rangle\right)^2}, \tag{21}$$

where the sums and the averages $\langle \ldots \rangle$ are performed over space. Similar definitions apply to other components, and allow us to define an aggregate coefficient of determination R^2_σ averaged over all stress components. Accurate estimates correspond to numerical values of R^2_σ close to 1. The discretized force balance Eqs. 5 and 6, used as a definition of inferred traction forces, yield a set $\{t^{\text{inf}}\}$ of inferred traction forces computed from the set of inferred stresses $\{\sigma^{\text{inf}}\}$. Comparing $\{t^{\text{num}}\}$ with $\{t^{\text{inf}}\}$ allows us to define similarly a R^2_T diagnostic for numerical data.

When analyzing an experimental data set $\{t^{\text{exp}}\}$ of traction forces, R^2_σ cannot be computed in the absence of a reference set of stresses. As above, comparing $\{t^{\text{exp}}\}$ with $\{t^{\text{inf}}\}$ allows us to define a measure of accuracy for experimental data, the coefficient of determination R^2_T. An alternative measure of predictive accuracy is the χ^2_T diagnostic, defined as the average value of the square of reduced residuals

$$\chi^2_T = \frac{1}{2N} \sum \frac{\left(t^{\text{exp}} - t^{\text{inf}}\right)^2}{\delta \widehat{T}^2}, \tag{22}$$

where the sum is performed over space and over traction force components. This measure of accuracy is, up to a normalizing factor, similar to the "omnibus goodness-of-fit" measure advocated in the literature (56,57). The estimated standard deviation $\delta \widehat{T}$ may be replaced in Eq. 22 by the measurement error δt. Numerical values of χ^2_T close to 0 are indicators of high accuracy.

A last test of accuracy is provided by the calculation of average experimental stress values from traction force data (53), which may be compared with the average inferred stresses for each component (see S3.4 and S1.4).

Experimental methods

We used Madin-Darby canine kidney (MDCK) cells as an epithelial cell model.

Cell culture

MDCK wild-type cells were cultured in media containing DMEM (Life Technologies, Carlsbad, CA), 10% FBS (Life Technologies), and 1% antibiotics (penicillin and streptomycin).

Microcontact printing and substrate preparation for traction force microscopy

We measured the traction forces exerted by cells on their substrate by using soft silicone gel as previously described in Vedula et al. (58). Fluorescent beads were deposited onto the gel to measure the displacement field. Briefly, a thin layer of the gel was spread on a glass-bottom dish and then cured at 80°C for 2 h. Cured gel was silanized using a 5% solution of APTES ((3-aminopropyl) triethoxysilane; Sigma-Aldrich, St. Louis, MO) in pure ethanol. This gel was later incubated for 5 min with 100 nm carboxylated fluorescent beads (Invitrogen, Carlsbad, CA) suspended in deionized water. Subsequently, the substrate was dried and microcontact-printed with fibronectin (13,59) using a thin water-soluble PVA (polyvinyl alcohol) membrane that allows the transfer of fibronectin on soft gel. The PVA membrane was later dissolved and the non-contact-printed areas were blocked using 0.2% pluronics (Sigma-Aldrich) solution. The substrate was then washed and was seeded with cells. Cells were allowed to grow until the microcontact printed area was fully covered.

The images were acquired using phase contrast and fluorescent channels to record cell positions and bead displacements, respectively.

For analysis, the imaging drifts were corrected in ImageJ (National Institutes of Health, Bethesda, MD) using the Image Stabilizer plugin (60). To analyze the displacement field of beads, we used an open-source iterative particle-image velocimetry plugin in ImageJ (61). To reconstruct the traction force field from the obtained displacement field, an open source Fourier transform traction cytometry plugin was used in ImageJ (61). The resulting traction force values were taken for the validation of the BISM inferred stress fields. To estimate the experimental error δt_{exp} made on traction force measurements, we calculated the mean value of traction forces measured on square regions of the substrate devoid of cells (surface area $50 \times 50\ \mu\text{m}^2$).

Monolayer height measurement

The confluent cell monolayer was fixed for immunofluorescence microscopy. Actin present inside the cells was fluorescently labeled using Alexa Fluor 488-conjugated phalloidin (Invitrogen) at 1:1000 dilution in PBS. To measure tissue height, overall cell shape was then visualized with the help of cortical actin. Imaging was done using a model No. LSM 780 confocal microscope (Carl Zeiss, Jena, Germany) with a step size of 0.4 μm to capture the entire height of the tissue. In the confined ring-shape geometry, height was measured at different locations to obtain the mean value and standard deviation of the monolayer height $h = 5.3 \pm 1.2\ \mu$m.

RESULTS

Validation: numerical data

A first example of the application of BISM to a numerical data set is given by using the traction force field of a compressible viscous fluid driven by active force dipoles, interacting with its substrate through an effective fluid friction force, and confined in a square, with the boundary conditions (Eq. 4). We solve this problem on a $100 \times 100\ \mu\text{m}^2$ square over a regular Cartesian grid with $C = R = 50$, $N = C \times 2500$, and $l = 2\ \mu$m (see S1.1). We use material parameter values typical of cell monolayers: friction coefficient $\xi_v = 10^0$ kPa μm^{-1} s (7), shear viscosity $\eta = 10^3$ kPa μm s (62), and compression viscosity $\eta' = \eta$. To account for the measurement error, we add to the traction force field a white noise of relative amplitude 5% (variance $s^2_{\text{exp}} = 1.2\ 10^{-3}$ kPa^2), and obtain the numerical data set $\{t^{\text{num}}\}$ of traction forces (Fig. 3 *a*), referred to below as "Viscous". We checked that the total sum of the traction forces is close to zero, as expected for a closed system with negligible inertia.

Bayesian inversion is performed with a custom-made script written in MATLAB (The MathWorks, Natick, MA). With $s^2_{(0)} = 10^{-1}$ kPa^2 and $s^2_{0(0)} = 10^2$ kPa^2 μm^2 as initial values, the resolution method converges in a few steps toward the asymptotic hyperparameter values $s^2_{(\infty)} = 4.7\ 10^{-7}$ kPa^2 and $s^2_{0(\infty)} = 3.4\ 10^{-1}$ kPa^2 μm^2, or $\Lambda_{(\infty)} = 5.5\ 10^{-6}$ (see S3.1 and Fig. S4 *a* in the Supporting Material). The data sets $\{\sigma^{\text{num}}\}$ and $\{\sigma^{\text{inf}}\}$ of simulated and inferred stresses are shown in Fig. 3, *b* and *c*: we find that their spatial structures are quite similar. This observation is confirmed quantitatively by plotting component by component the inferred stress versus the simulated stress (Fig. 3, *d–f*), and by the numerical values of the coefficients of determination $R^2_{xx} = 0.94$, $R^2_{yy} = 0.97$, $R^2_{xy} = 0.95$, yielding an aggregate measure of accuracy $R^2_\sigma = 0.96$, close to 1. Using the inferred data set $\{t^{\text{inf}}\}$ of traction forces, we also obtain

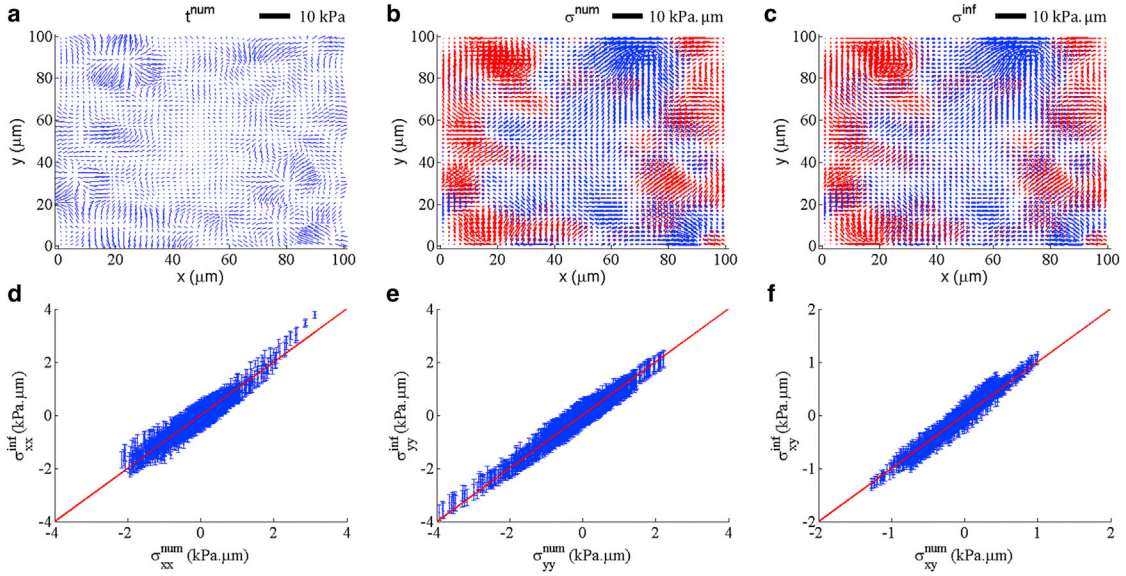

FIGURE 3 Validation: numerical data. (*a*) Simulated traction force field t^{num}, represented at each point by an arrow. Scale bar: 10 kPa. (*b*) Simulated stress field σ^{num}. (*c*) Inferred stress field σ^{inf}, plotted on a 50×50 grid. At each point, the stress tensor is represented by two line segments oriented along the stress eigenvectors, of lengths proportional to the eigenvalues (*blue*, tensile stress; *red*, compressive stress; scale bar: 10 kPa μm). Note the high degree of similarity between images (*b*) and (*c*). (*d–f*) Plots of the inferred stress versus the simulated stress for each component, in kPa.μm. Error bars correspond to $\delta\widehat{\sigma}$ and the red line is the bisector $y = x$. To see this figure in color, go online.

$1 - R_T^2 = 2\ 10^{-5}$ and $\chi_T^2 = 7\ 10^{-7}$, indicating that all the information contained in the traction force data is used. An order of magnitude of the error bar is given by the standard deviations, calculated using Eq. 16: $\delta\widehat{\sigma} \approx 10^2\ ls_{(\infty)} \approx 10^{-1}$ kPa μm, corresponding to $\approx 10\%$ of the maximal stresses.

All qualitative and quantitative indicators show that the stress field has been inferred accurately.

Robustness to variations of the statistical model

We test the robustness of BISM by varying one by one each feature of the statistical model, first focusing on alternative definitions of the prior, arguably our most prominent assumption; and second, modifying the likelihood, the hyperprior, and the resolution method. For conciseness, precise definitions and implementations are given in S2.1–S2.3. Table S1 in the Supporting Material lists the values of R_σ^2 thus obtained, given the same numerical data sets as for BISM.

Setting α_{xy} to 0 in the definition of the prior has a significant influence on the accuracy of inference $(R_\sigma^2 = 0.75)$: the symmetry of the stress tensor needs to be enforced in the prior for accurate estimation. Unsurprisingly, this impacts less the diagonal $(R_{xx}^2 = R_{yy}^2 = 0.81)$ than the shear components $(R_{xy}^2 = R_{yx}^2 = 0.61)$. In a similar way, knowledge of the correct boundary conditions should be included in the prior whenever possible: setting α_{BC} to 0 has a large negative impact $(R_\sigma^2 = 0.53)$. We shall further comment below on the influence of boundary conditions.

Importantly, the accuracy of inference remains excellent when the prior, the likelihood, or the hyperprior distributions are not Gaussian. This shows that the accuracy of BISM does not depend sensitively on a Gaussian assumption. Of note, we do not assume that traction force data obeys a Gaussian distribution. The data set ($\{t^{num}\}$ or $\{t^{exp}\}$) is used as is—indeed, experimental traction force distributions are known to exhibit exponential tails (5,63). In all cases, the regularization parameter is small $\Lambda_{(\infty)} \ll 1$ (see Table S3): the distribution of inferred stresses $\{\sigma^{inf}\}$ depends mostly on the empirical distribution of traction force data. Thus, even if the multivariate posterior distribution is Gaussian, the univariate, empirical distribution of the inferred stress (the mode $\vec{\sigma}_{\Pi\,(\infty)}$) is not necessarily Gaussian (see Fig. S7 for numerical data). Similarly, even if the stress prior distribution function has a zero mean, the mean inferred stress is not necessarily equal to zero (see Fig. 5 *i*, later, for an example). The small values of $\Lambda_{(\infty)}$ are consistent with robustness, with respect to variations of the prior.

We conclude that BISM is robust to variations of the statistical model.

Robustness to variations of the numerical simulation

We next apply BISM to a broad spectrum of numerical data, and vary successively the values of material parameters, the rheology, the boundary conditions, the system shape, the

spatial resolution, the nature, and the amplitude of the measurement noise (see S2.2).

Given the values of R_σ^2 compiled in Table S2, we verify that BISM remains accurate with a different (elastic) rheology (also see *Elastic 1* in Table 1), or in a different (circular) geometry. In the viscous case, we observe that the accuracy decreases as a function of the bulk viscosity η'. For larger η', we observe larger values of stress components, leading to asymmetrical distributions: this is at variance with our assumption of an even prior distribution, and may explain the lower value of R_σ^2 obtained when $\eta' = 10^1\ \eta$.

Accuracy decreases when the prior does not include our knowledge of the boundary conditions. However, the influence of erroneous values of the stress at the system's boundaries rapidly decreases far from the edge. When the coefficient α_{BC} is set to 0, removing the outermost rows and columns increases R_σ^2 from 0.53 to 0.60. We estimate the corresponding penetration length of boundary values to ~10% of the system size, consistent with Tambe et al. (34). We conclude that, whenever available, the correct boundary conditions should be taken into account in the prior.

Importantly (see Fig. 4), accuracy remains acceptable $(R_\sigma^2 > 0.8)$ for a spatial resolution larger than a few data points per cell, as well as for measurement noise levels up to 20% of the traction force amplitude, consistent with measurement errors typical of force traction microscopy (31).

These results highlight that BISM is robust to variations of the numerical simulations that yield the traction force data.

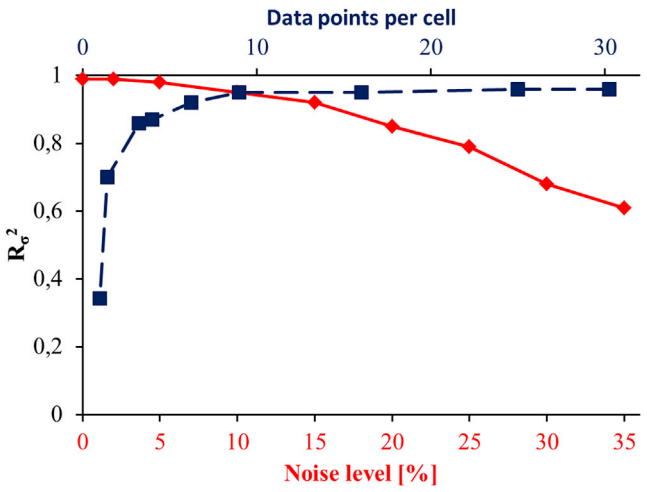

FIGURE 4 Robustness. BISM remains highly accurate $(R_\sigma^2 > 0.8)$ for noise levels and spatial resolutions typical of traction force measurements. (*Red solid line*) Coefficient of determination R_σ^2 versus relative level of added noise. R_σ^2 is averaged over three realizations of the noise. (*Blue dashed line*) Coefficient of determination R_σ^2 versus number of traction force data points per cell, for a typical cell area of 100 μm^2. To see this figure in color, go online.

Validation: experimental data

While inverting the force balance equations (Eq. 1) requires specific techniques in two dimensions, the same problem reduces in one dimension to straightforward integration along the spatial coordinate (5). For this reason, we fabricated a micropatterned ring whose measured mean radius $r_{mean} = 90\ \mu m$ is larger than its width $w = 33\ \mu m$; measured the substrate displacement field; and deduced the traction forces exerted by a monolayer of MDCK cells confined within the ring (Figs. 5, *a–c*, and see Experimental Methods for further details). We find an average traction force amplitude $t_{exp} \approx 200$ Pa for a measurement error of the order of $\delta t_{exp} \approx 40$ Pa, and deduce a relative error $\delta t_{exp}/t_{exp}$ of ~20%, consistent with the range of noise amplitudes where BISM was deemed applicable (see Fig. 4). The height of the monolayer is typically $5.3 \pm 1.2\ \mu m$ (see Experimental Methods), much smaller than the spatial extension $2\pi r_{mean}$, and varies smoothly (see Fig. S8). In Fig. 5, *d–f*, we plot the three stress components as inferred by BISM, with a regularization parameter $\Lambda_{(\infty)} = 6.7\ 10^{-6}$ and a traction force-based measure of accuracy $\chi_T^2 = 4.7\ 10^{-6}$, as defined by Eq. 22. Note that the inferred stresses are mostly positive, even though the prior distribution is a zero-mean Gaussian (see Fig. 5 *i*).

Because shear stresses are small compared to angular normal stresses $|\sigma_{r\theta}|, |\sigma_{\theta r}| \ll |\sigma_{\theta\theta}|$, the orthoradial component of the force balance equation (see S1.2) simplifies to

$$\frac{\partial \sigma_{\theta\theta}}{\partial \theta} = r\, t_\theta. \tag{23}$$

Taking into account the experimental angular resolution $\Delta\theta$, and averaging radially over the width of the ring, we obtain the 1D value of the increment of orthoradial stress over $\Delta\theta$:

$$\Delta\sigma_{\theta\theta}^{1D} = \langle r\, t_\theta \rangle_r\, \Delta\theta. \tag{24}$$

This value is compared with the radially averaged increment of orthoradial stress inferred by BISM $\langle \Delta\sigma_{\theta\theta} \rangle_r$ (Fig. 5, *g* and *h*). The excellent agreement found between experimental $(\langle r\, t_\theta \rangle_r\, \Delta\theta)$ and inferred $(\langle \Delta\sigma_{\theta\theta} \rangle_r)$ 1D stresses is quantified by a coefficient of determination $R_{ring}^2 = 0.99$ (see Fig. 5 *h*). To check that BISM allows us to infer absolute stress values, we calculate the average pressure $\langle P_{exp} \rangle$ from traction force data (see S1.4):

$$\langle P_{exp} \rangle = \frac{1}{2} \langle t_r r \rangle, \tag{25}$$

where $\langle\rangle$ denotes spatial averaging over the whole domain. We obtain $\langle P_{exp} \rangle = -2.18$ kPa.μm, in agreement with the average inferred pressure $\langle P_{inf} \rangle = -2.17 \pm 0.94$ kPa.μm.

We conclude that BISM is readily applicable to experimental traction force data, and has been validated on

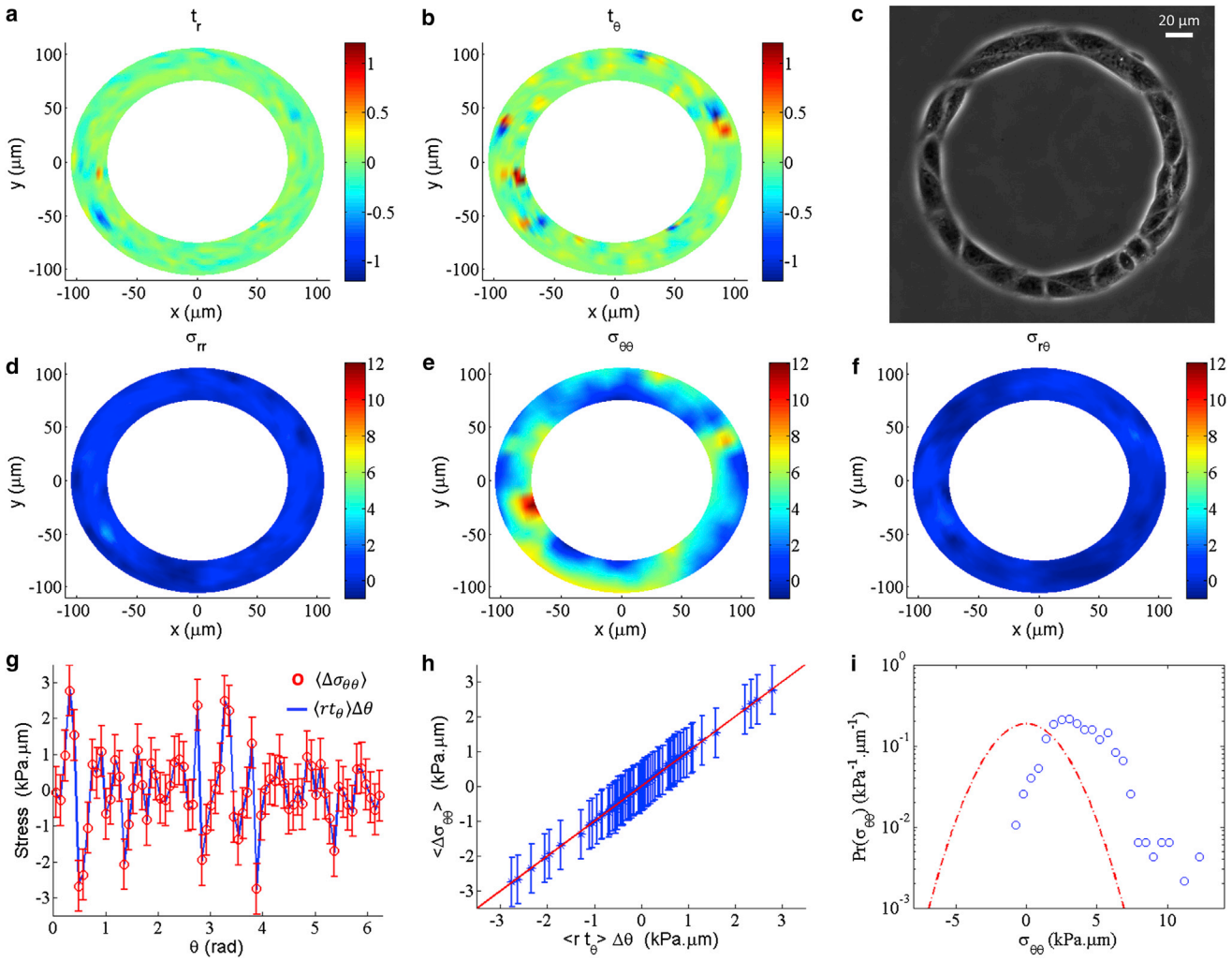

FIGURE 5 Validation: experimental data. (*a* and *b*) Heat maps of the components t_r and t_θ of the traction forces $t^{\exp}$ in kPa, on a 12×72 polar grid. (*c*) Phase constrast image of the MDCK cell monolayer. Scale bar: 20 μm. (*d–f*) Heat maps of the components σ_{rr}, $\sigma_{\theta\theta}$, and $\sigma_{r\theta}$ of the inferred stress field $\sigma^{\inf}$ in kPa μm. (*g*) Angular profiles of the radially averaged inferred stress ($\langle \Delta\sigma_{\theta\theta} \rangle_r$, *red circles*) and of the 1D stress ($\langle r\, t_\theta \rangle_r\, \Delta\theta$, *blue line*), with an angular resolution $\Delta\theta = \pi/36$ rad. Error bars of the inferred stress are the radial average of $\delta\widehat{\sigma}_{\theta\theta}$. (*h*) Radially averaged inferred stress versus the 1D stress. The coefficient of determination of this plot is $R^2_{\text{ring}} = 0.99$. (*i*) Empirical distribution function of the inferred component $\sigma_{\theta\theta}$ (*blue circles*). Red dashed line corresponds to the zero-mean, Gaussian prior distribution function with standard deviation $s_0 = 2.13$ kPa.μm. To see this figure in color, go online.

experimental data without reference to a specific rheological model of the tissue.

Comparison with monolayer stress microscopy

Monolayer stress microscopy, as introduced in Tambe et al. (26), assumes that the cell monolayer is a linear, isotropic elastic body. Given traction force data, MSM consists in finding the stress field that minimizes an energy functional of the cell monolayer. MSM is thus straightforward to implement using FreeFem++ (64), a finite element software based on the same variational approach (see S1.1).

A simpler implementation of MSM, which also assumes an elastic cell monolayer rheology, has been proposed recently in Moussus et al. (36). We call this method "MSMu" because it does not require the calculation of traction forces and uses the substrate displacement field u as input data. MSMu further assumes that the displacement field u is continuous at the interface between substrate and cells: tissue internal stresses are computed directly from substrate displacements. In practice, we calculate substrate displacements from the traction force data set, given numerical values of the substrate elastic modulus $E_{\text{sub}} = 5$ kPa and Poisson ratio $\nu_{\text{2D sub}} = 0.5$ (36).

By analogy with MSM, we introduce a stress estimation method, named "MSMη", that assumes a viscous rheology for the cell monolayer. Thanks to the variational formulation, we compute the velocity field given the force traction field with FreeFem++, and estimate the stress field given numerical values of the viscosity coefficients. Of note, other

variants of MSM could be implemented assuming other tissue rheologies consistent with a variational formulation (65).

The comparison relies on three numerical simulations: in addition to the Viscous and Elastic 1 data sets studied above, another simulation of an elastic tissue, named Elastic 2, has been performed, using the elastic coefficients $E = 10$ kPa μm and $\nu_{2D} = 0.5$, as advocated in Moussus et al. (36). Each variant of MSM assumes a tissue rheology, and thus relies on a set of material parameters. To perform MSM and MSMu, we use the same tissue elastic coefficients as in the Elastic 1 (26) and Elastic 2 (36) simulations, respectively. To perform MSMη, we use the same tissue viscosity coefficients as in the Viscous simulation.

Table 1 summarizes our results and compares the accuracy of the different methods (see also Fig. S9 for visual comparison). In all cases, the values of R^2_σ are closer to 1 for BISM, which performs better than MSM, MSMu, and MSMη. By construction, BISM seems less sensitive to experimental noise than deterministic stress microscopies. For each variant of MSM, accuracy is maximal for the data set generated according to the same rheological hypothesis, i.e., Elastic 1, Elastic 2, and Viscous for MSM, MSMu, and MSMη, respectively. Unsurprisingly, a mismatch between numerical simulation and stress microscopy methods, either in the values of material parameters or in the choice of a rheology, leads to a lower value of the coefficient of determination.

We also applied MSM to the experimental data set studied in Validation: Experimental Data. Following the same protocol, we obtained a larger dispersion of inferred values than with BISM. The inferred data set obtained by MSM is characterized by a lower coefficient of determination $R^2_{\text{ring}} = 0.32$, far below the BISM value $R^2_{\text{ring}} = 0.99$.

All existing stress microscopies infer the stress field up to an additive null vector σ^0 such that div $\sigma^0 = 0$. Classically (53), null vectors of the linear problem div $\sigma = \vec{t}$ are related to the Airy stress function χ through $\sigma^0_{xx} = (\partial^2\chi/\partial y^2)$, $\sigma^0_{yy} = (\partial^2\chi/\partial x^2)$, and $\sigma^0_{xy} = -(\partial^2\chi/\partial x\partial y)$. Because BISM infers faithfully the mean stress $\langle\sigma\rangle$ in confined geometries, it limits the class of undetectable stresses to zero-mean stress fields that verify both div $\sigma^0 = 0$ and the boundary conditions (Eq. 4). Alternative methods will be necessary to ascertain the relevance of these special solutions to cell monolayer mechanics.

TABLE 1 Comparison with monolayer stress microscopy

Rheology	BISM	MSM	MSMu	MSMη
Viscous	0.96	−0.52	0.48	0.91
Elastic 1	0.97	0.88	0.73	0.80
Elastic 2	0.99	0.61	0.85	0.67

Coefficients of determination R^2_σ obtained with BISM, MSM, MSMu, and MSMη (see text for definitions). Traction force data sets were obtained with material parameter values $\eta = 10^3$ kPa μm s, $\eta' = \eta$ (*Viscous*); $E = 10^2$ kPa μm, $\nu_{2D} = 0.5$ (26) (*Elastic 1*); and $E = 10$ kPa μm, $\nu_{2D} = 0.5$ (36) (*Elastic 2*). A white noise of relative amplitude 5% is added in all cases.

CONCLUSION

Bayesian inversion stress microscopy estimates the internal stress field of a cell monolayer given traction force data. Validation on both numerical and experimental data shows that the method works reliably independently of the tissue rheology, of its geometry, and of the boundary conditions imposed on the stress field. As a consequence, BISM should apply equally well to isolated cell assemblies and to patches of cells within a larger monolayer. Because the hypotheses made pertain to statistics (Bayesian inversion), we checked that the method is robust to changes in the underlying statistical model, in particular to changes in the prior. Importantly, its statistical nature leads to a simple, natural definition of an error bar on the stress estimate. It is compatible with the level of experimental noise and with the spatial resolution typical of traction force microscopy. Last, BISM is more accurate than MSM, and its accuracy is less sensitive to the rheology of the tissue than all variants of monolayer stress microscopy. BISM is quite general because it relies on the laws of mechanics and on reasonable and robust statistical assumptions. It can therefore be applied to other active materials strongly interacting with a soft substrate, provided the height of the system is small compared to its planar spatial extension.

We analyzed traction force images, i.e., spatial data at a given, fixed time. However, BISM does not rely on an assumption of quasi-stationarity, and would apply equally well to spatio-temporal data, i.e., to traction force movies. Our preliminary results suggest that combining Bayesian inversion with Kalman filtering then further improves accuracy.

To date, the modeling of cell monolayer mechanics typically relies on a forward approach: assumptions made on tissue rheology are validated indirectly through predictions made on (measurable) tissue kinematics. A reliable measurement of the internal stress field paves the way to inverse approaches, where the combination of stress with kinematic data, such as the strain rate field or the cell-neighbor exchange rate field, would allow us to read out constitutive equations from data, and to infer the values of material parameters.

SUPPORTING MATERIAL

Supporting Materials and Methods, three tables, and nine figures are available at http://www.biophysj.org/biophysj/supplemental/S0006-3495(16)30042-X.

AUTHOR CONTRIBUTIONS

C.T.L., S.I., B.L., and P.M. conceived and designed research; V.N., S.J., and P.M. performed research; V.N. and S.J. analyzed the data; and V.N., B.L., and P.M. wrote the article.

ACKNOWLEDGMENTS

We thank Cyprien Gay, François Graner, Yohei Kondo, and Sham Tlili for stimulating discussions.

Financial supports from the Human Frontier Science Program (grant No. RGP0040/2012), the European Research Council under the European Union's Seventh Framework Program (No. FP7/2007-2013)/ERC grant agreement No. 617233, and the Mechanobiology Institute are gratefully acknowledged. S.J. acknowledges the Merlion-2014 program of the French Ministry of Foreign Affairs. B.L. acknowledges the Institut Universitaire de France.

SUPPORTING CITATIONS

References (66–75) appear in the Supporting Material.

REFERENCES

1. Keller, R., L. Davidson, …, P. Skoglund. 2000. Mechanisms of convergence and extension by cell intercalation. *Phil. Trans. R. Soc. Lond. B.* 355:897–922.
2. van der Flier, L. G., and H. Clevers. 2009. Stem cells, self-renewal, and differentiation in the intestinal epithelium. *Annu. Rev. Physiol.* 71:241–260.
3. Friedl, P., and D. Gilmour. 2009. Collective cell migration in morphogenesis, regeneration and cancer. *Nat. Rev. Mol. Cell Biol.* 10:445–457.
4. Poujade, M., E. Grasland-Mongrain, …, P. Silberzan. 2007. Collective migration of an epithelial monolayer in response to a model wound. *Proc. Natl. Acad. Sci. USA.* 104:15988–15993.
5. Trepat, X., M. R. Wasserman, …, J. J. Fredberg. 2009. Physical forces during collective cell migration. *Nat. Phys.* 5:426–430.
6. Anon, E., X. Serra-Picamal, …, B. Ladoux. 2012. Cell crawling mediates collective cell migration to close undamaged epithelial gaps. *Proc. Natl. Acad. Sci. USA.* 109:10891–10896.
7. Cochet-Escartin, O., J. Ranft, …, P. Marcq. 2014. Border forces and friction control epithelial closure dynamics. *Biophys. J.* 106:65–73.
8. Vedula, S. R., M. C. Leong, …, B. Ladoux. 2012. Emerging modes of collective cell migration induced by geometrical constraints. *Proc. Natl. Acad. Sci. USA.* 109:12974–12979.
9. Marel, A.-K., M. Zorn, …, J. O. Rädler. 2014. Flow and diffusion in channel-guided cell migration. *Biophys. J.* 107:1054–1064.
10. Doxzen, K., R. K. V. Sri, …, C. T. Lim. 2013. Guidance of collective cell migration by substrate geometry. *Integr. Biol.* 5:1026–1035.
11. Deforet, M., V. Hakim, …, P. Silberzan. 2014. Emergence of collective modes and tri-dimensional structures from epithelial confinement. *Nat. Commun.* 5:3747.
12. Ashby, W. J., and A. Zijlstra. 2012. Established and novel methods of interrogating two-dimensional cell migration. *Integr. Biol.* (*Camb.*). 4:1338–1350.
13. Vedula, S. R., A. Ravasio, …, B. Ladoux. 2013. Collective cell migration: a mechanistic perspective. *Physiology* (*Bethesda*). 28:370–379.
14. Ladoux, B., and A. Nicolas. 2012. Physically based principles of cell adhesion mechanosensitivity in tissues. *Rep. Prog. Phys.* 75:116601.
15. Liu, Z., J. L. Tan, …, C. S. Chen. 2010. Mechanical tugging force regulates the size of cell-cell junctions. *Proc. Natl. Acad. Sci. USA.* 107:9944–9949.
16. Bazellières, E., V. Conte, …, X. Trepat. 2015. Control of cell-cell forces and collective cell dynamics by the intercellular adhesome. *Nat. Cell Biol.* 17:409–420.
17. K. Sugimura, F. Graner, and P.-F. Lenne. 2015. Measuring forces and stresses in situ in living tissues. 2016. Dev. 143:186–196.
18. Grashoff, C., B. D. Hoffman, …, M. A. Schwartz. 2010. Measuring mechanical tension across vinculin reveals regulation of focal adhesion dynamics. *Nature.* 466:263–266.
19. Borghi, N., M. Sorokina, …, A. R. Dunn. 2012. E-cadherin is under constitutive actomyosin-generated tension that is increased at cell-cell contacts upon externally applied stretch. *Proc. Natl. Acad. Sci. USA.* 109:12568–12573.
20. Kole, T. P., Y. Tseng, and D. Wirtz. 2004. Intracellular microrheology as a tool for the measurement of the local mechanical properties of live cells. *Methods Cell Biol.* 78:45–64.
21. Tanase, M., N. Biais, and M. Sheetz. 2007. Magnetic tweezers in cell biology. *Methods Cell Biol.* 83:473–493.
22. Campàs, O., T. Mammoto, …, D. E. Ingber. 2014. Quantifying cell-generated mechanical forces within living embryonic tissues. *Nat. Methods.* 11:183–189.
23. Nienhaus, U., T. Aegerter-Wilmsen, and C. M. Aegerter. 2009. Determination of mechanical stress distribution in *Drosophila* wing discs using photoelasticity. *Mech. Dev.* 126:942–949.
24. Rauzi, M., P. Verant, …, P.-F. Lenne. 2008. Nature and anisotropy of cortical forces orienting *Drosophila* tissue morphogenesis. *Nat. Cell Biol.* 10:1401–1410.
25. Bonnet, I., P. Marcq, …, F. Graner. 2012. Mechanical state, material properties and continuous description of an epithelial tissue. *J. R. Soc. Interface.* 9:2614–2623.
26. Tambe, D. T., C. C. Hardin, …, X. Trepat. 2011. Collective cell guidance by cooperative intercellular forces. *Nat. Mater.* 10:469–475.
27. Ambrosi, D., A. Duperray, …, C. Verdier. 2009. Traction patterns of tumor cells. *J. Math. Biol.* 58:163–181.
28. Style, R. W., R. Boltyanskiy, …, E. R. Dufresne. 2014. Traction force microscopy in physics and biology. *Soft Matter.* 10:4047–4055.
29. Dembo, M., and Y. L. Wang. 1999. Stresses at the cell-to-substrate interface during locomotion of fibroblasts. *Biophys. J.* 76:2307–2316.
30. Butler, J. P., I. M. Tolić-Nørrelykke, …, J. J. Fredberg. 2002. Traction fields, moments, and strain energy that cells exert on their surroundings. *Am. J. Physiol. Cell Physiol.* 282:C595–C605.
31. Sniadecki, N. J., and C. S. Chen. 2007. Microfabricated silicone elastomeric post arrays for measuring traction forces of adherent cells. *Methods Cell Biol.* 83:313–328.
32. du Roure, O., A. Saez, …, B. Ladoux. 2005. Force mapping in epithelial cell migration. *Proc. Natl. Acad. Sci. USA.* 102:2390–2395.
33. Saez, A., E. Anon, …, B. Ladoux. 2010. Traction forces exerted by epithelial cell sheets. *J. Phys. Condens. Matter.* 22:194119.
34. Tambe, D. T., U. Croutelle, …, J. J. Fredberg. 2013. Monolayer stress microscopy: limitations, artifacts, and accuracy of recovered intercellular stresses. *PLoS One.* 8:e55172.
35. Zimmermann, J., R. L. Hayes, …, H. Levine. 2014. Intercellular stress reconstitution from traction force data. *Biophys. J.* 107:548–554.
36. Moussus, M., C. der Loughian, …, A. Nicolas. 2014. Intracellular stresses in patterned cell assemblies. *Soft Matter.* 10:2414–2423.
37. Ranft, J., M. Basan, …, F. Jülicher. 2010. Fluidization of tissues by cell division and apoptosis. *Proc. Natl. Acad. Sci. USA.* 107:20863–20868.
38. Arciero, J. C., Q. Mi, …, D. Swigon. 2011. Continuum model of collective cell migration in wound healing and colony expansion. *Biophys. J.* 100:535–543.
39. Lee, P., and C. W. Wolgemuth. 2011. Crawling cells can close wounds without purse strings or signaling. *PLOS Comput. Biol.* 7:e1002007.
40. Köpf, M. H., and L. M. Pismen. 2012. A continuum model of epithelial spreading. *Soft Matter.* 9:3727–3734.
41. Vedula, S. R., H. Hirata, …, B. Ladoux. 2014. Epithelial bridges maintain tissue integrity during collective cell migration. *Nat. Mater.* 13:87–96.
42. Kaipio, J., and E. Somersalo. 2006. Statistical and Computational Inverse Problems. Springer, New York.

43. Stuart, A. M. 2010. Inverse problems: a Bayesian perspective. *Acta Numer.* 19:451–559.

44. von Toussaint, U. 2011. Bayesian inference in physics. *Rev. Mod. Phys.* 83:943–999.

45. Kimura, A., A. Celani, …, K. Nakamura. 2015. Estimating cellular parameters through optimization procedures: elementary principles and applications. *Front. Physiol.* 6:60.

46. Dembo, M., T. Oliver, …, K. Jacobson. 1996. Imaging the traction stresses exerted by locomoting cells with the elastic substratum method. *Biophys. J.* 70:2008–2022.

47. Soiné, J. R., C. A. Brand, …, U. S. Schwarz. 2015. Model-based traction force microscopy reveals differential tension in cellular actin bundles. *PLOS Comput. Biol.* 11:e1004076.

48. Ishihara, S., and K. Sugimura. 2012. Bayesian inference of force dynamics during morphogenesis. *J. Theor. Biol.* 313:201–211.

49. Sugimura, K., and S. Ishihara. 2013. The mechanical anisotropy in a tissue promotes ordering in hexagonal cell packing. *Development.* 140:4091–4101.

50. Ishihara, S., K. Sugimura, …, F. Graner. 2013. Comparative study of non-invasive force and stress inference methods in tissue. *Eur. Phys. J. E Soft Matter.* 36:9859.

51. Chiou, K. K., L. Hufnagel, and B. I. Shraiman. 2012. Mechanical stress inference for two dimensional cell arrays. *PLOS Comput. Biol.* 8:e1002512.

52. Brodland, G. W., J. H. Veldhuis, …, M. S. Hutson. 2014. CellFIT: a cellular force-inference toolkit using curvilinear cell boundaries. *PLoS One.* 9:e99116.

53. Landau, L. D., and E. M. Lifshitz. 1975. Elasticity Theory. Pergamon Press, New York.

54. Zehnder, S. M., M. Suaris, …, T. E. Angelini. 2015. Cell volume fluctuations in MDCK monolayers. *Biophys. J.* 108:247–250.

55. Schwarz, U. S., N. Q. Balaban, …, S. A. Safran. 2002. Calculation of forces at focal adhesions from elastic substrate data: the effect of localized force and the need for regularization. *Biophys. J.* 83:1380–1394.

56. Carlin, B. P., and T. A. Louis. 2008. Bayesian Methods for Data Analysis, 3rd Ed. Chapman & Hall/CRC, Boca Raton, FL.

57. Gelman, A., J. B. Carlin, …, D. B. Rubin. 2014. Bayesian Data Analysis. Taylor & Francis, Boca Raton, FL.

58. Vedula, S. R., A. Ravasio, …, B. Ladoux. 2014. Microfabricated environments to study collective cell behaviors. *Methods Cell Biol.* 120:235–252.

59. Fink, J., M. Théry, …, M. Piel. 2007. Comparative study and improvement of current cell micro-patterning techniques. *Lab Chip.* 7:672–680.

60. K Li. 2008. The Image Stabilizer for ImageJ. http://www.cs.cmu.edu/~kangli/code/Image_Stabilizer.html.

61. Martiel, J.-L., A. Leal, …, M. Théry. 2015. Measurement of cell traction forces with ImageJ. *Methods Cell Biol.* 125:269–287.

62. Harris, A. R., L. Peter, …, G. T. Charras. 2012. Characterizing the mechanics of cultured cell monolayers. *Proc. Natl. Acad. Sci. USA.* 109:16449–16454.

63. Gov, N. S. 2009. Traction forces during collective cell motion. *HFSP J.* 3:223–227.

64. Hecht, F. 2012. New development in FreeFem++. *J. Numer. Math.* 20:251–266.

65. Tlili, S., C. Gay, …, P. Saramito. 2015. Colloquium: Mechanical formalisms for tissue dynamics. *Eur. Phys. J. E Soft Matter.* 38:121.

66. Landau, L. D., and E. M. Lifshitz. 1987. Fluid Mechanics. Pergamon Press, New York.

67. Jenkins, A. D., and K. B. Dysthe. 1997. The effective film viscosity coefficients of a thin floating fluid layer. *J. Fluid Mech.* 109:108101.

68. Tarantola, A. 2005. Inverse Problem Theory and Methods for Model Parameter Estimation. SIAM: Society for Industrial and Applied Mathematics, Philadelphia, PA.

69. McLachlan, G. J., and T. Krishnan. 2008. The EM Algorithm and Its Extensions. Wiley-Interscience, New York.

70. Delarue, M., J.-F. Joanny, …, J. Prost. 2014. Stress distributions and cell flows in a growing cell aggregate. *Interface Focus.* 4:20140033.

71. Banerjee, S., and M. C. Marchetti. 2012. Contractile stresses in cohesive cell layers on finite-thickness substrates. *Phys. Rev. Lett.* 109:108101.

72. Eltoft, T., T. Kim, and T.-W. Lee. 2006. On the multivariate Laplace distribution. *Signal Proc. Lett. IEEE.* 13:300–303.

73. Beal, M. J. 2003. Variational algorithms for approximate Bayesian inference. PhD thesis, Gatsby Computational Neuroscience Unit, University College London, London, UK.

74. Tipping, M. E. 2001. Sparse Bayesian learning and the relevance vector machine. *J. Mach. Learn. Res.* 1:211–244.

75. Hansen, P. C. 1992. Analysis of discrete ill-posed problems by means of the L-curve. *SIAM Rev.* 34:561–580.